ELSEVIER

Ceramics International 30 (2004) 515–523

CERAMICS INTERNATIONAL

www.elsevier.com/locate/ceramint

Characterization of the Y–Fe–O ultrafine particles containing a new compound $YFe_{(3+x)}O_{1.5(4+x)}$ synthesized by rf thermal plasmas

M. Sugasawa [a,*], N. Kikukawa [a], Y. Nagano [a], N. Kayano [b], T. Kimura [b]

[a] *National Institute of Advanced Industrial Science and Technology, 16-1 Onogawa, Tsukuba, Japan*
[b] *Shibaura Institute of Technology, 3-9-14 Shibaura, Minato, Tokyo, Japan*

Received 8 July 2003; received in revised form 24 July 2003; accepted 25 August 2003

Abstract

We synthesized Y–Fe–O ultrafine particles that contained $YFe_{(3+x)}O_{1.5(4+x)}$, h-$YFeO_3$, ε-Fe_2O_3, and γ-Fe_2O_3, by using an rf Ar–O_2 thermal plasma evaporation method. The particles were characterized by using X-ray diffraction (XRD), transmission electron microscopy (TEM)/selected-area diffraction (SAD), inductively coupled plasma emission spectroscopy (ICP-ES), vibrating sample magnetometer (VSM) and Mössbauer spectrometry. $YFe_{(3+x)}O_{1.5(4+x)}$ is a new compound that has not yet been registered in the Powder Diffraction File (PDF) database. Because $YFe_{(3+x)}O_{1.5(4+x)}$ has a long-period, face-centered cubic structure, the maximum XRD peak was indexed by (444). The magnetic hysteresis loop measurements done by VSM showed that the particles contained either ferri- or ferromagnetic compounds. γ-Fe_2O_3 affected the saturation magnetization of the particles. However, we could not determine whether $YFe_{(3+x)}O_{1.5(4+x)}$ is a ferri- or ferromagnetic compound, by using XRD, VSM, or Mössbauer spectrometry. Therefore, the magnetic properties of $YFe_{(3+x)}O_{1.5(4+x)}$ should be further investigated.

Keywords: C. Magnetic properties; Thermal plasma

1. Introduction

Yttrium is used in many functional materials, and one of the main applications is the use of Y_2O_3 as an optical glass constituent [1]. YVO_4, Y_2O_3, and Y_2O_2S together with Eu^{3+} have been used to make luminescent ions [1], which are often used in color television picture tubes. $YBa_2Cu_3O_x$ is a super conductive material [2]. YAG ($Y_3Al_5O_{12}$: yttrium aluminum garnet) is used to make solid lasers [2]. YIG ($Y_3Fe_5O_{12}$: yttrium iron garnet) containing Fe has magnetic bubble characteristics, and is used to make high-density integrated memory elements [1]. Therefore, it is essential to widen the yttrium application by synthesizing new compounds containing Y.

We used a high-frequency induction (rf) plasma to synthesize ultrafine particles that contain Y, Fe, and O. The compound we formed has not yet been registered in the Powder Diffraction File (PDF) database [3–8]. We synthesized particles by using an rf Ar–O_2 thermal plasma to evaporate co-precipitated powders containing Y and Fe. The evaporated Y, Fe, and O condensed to form the particles. X-ray diffraction (XRD) of the particles showed that they contained a new cubic crystal main-product with face-centered cubic lattices that were formed by Y and Fe atoms together with by-products such as Y_2O_3 and h-$YFeO_3$ [3]. However, large quantities of by-products such as Y_2O_3 and h-$YFeO_3$ were synthesized. This might be caused by the wide range of Fe/Y (molar ratio) of individual particles in the co-precipitated powder [4]. Therefore, to synthesize particles with the above new compound of a pure single phase, we supplied to the plasma mists of aqueous nitrate solutions of Y and Fe with fixed Fe/Y ratios. By controlling the Fe/Y ratio, we were able to produce particles with the new compound close to a pure single phase [3]. However, because the quantity of the mist was small compared to that of the powder precursor, the diameter of the synthesized particles was small. This caused poor crystallinity. For this reason, the XRD pattern of the particles was broad, suggesting that they contained other products. Therefore, amorphous citrate gel powders with nearly constant Fe/Y ratio in the individual particles

---

[*] Corresponding author. Tel.: +81-29-861-8182; fax: +81-29-861-8866.
E-mail address: m-sugasawa@aist.go.jp (M. Sugasawa).

0272-8842/$30.00 © 2004 Elsevier Ltd and Techna Group S.r.l. All rights reserved.
doi:10.1016/j.ceramint.2003.08.004

was supplied to the plasma [4]. As a result, the particles were larger than those produced by using the liquid mist as a precursor, and the crystallinity also improved. Moreover, controlling the Fe/Y ratio of the precursor permits a pure single phase to be formed, similar to using the liquid mist [4–6].

The particles were composed of $YFe_{(3+x)}O_{1.5(4+x)}$ and other compounds. Because the crystalline structure and magnetic properties of $YFe_{(3+x)}O_{1.5(4+x)}$ have not been reported in the open literature, we tried to determine the crystalline structure and magnetic properties of $YFe_{(3+x)}O_{1.5(4+x)}$ in the Y–Fe–O particles that we synthesized in this work.

2. Experimental

Fig. 1 shows a schematic diagram of the high-frequency induction thermal plasma torch [7,8] used in our experiments. The plasma torch is composed of a water-cooled, double quartz tube. The bulkhead and probe are made of copper, and the high-frequency coil is connected to a high-frequency power supply with a maximum plate power of 60 kW and operating at a frequency of 4 MHz. In this system the plasma gas (A) is supplied from the gap between the bulkhead and the probe and has a swirl component. The sheath gas (B, C) is supplied from the outer surface of the bulkhead. Gas B is supplied in the radial direction, and has no swirl component. Gas C is supplied tangential to the outer surface of the bulkhead and has a swirl component. Furthermore, the precursor and carrier gas (D) are supplied from the tip of the copper probe. In this study an atmospheric pressure Ar–O_2 thermal plasma was used. Gases B and C were a mixture of Ar and O_2, and gases A and D were pure Ar. Amorphous citrate gel powders were used as the precursor, with a constant Fe/Y ratio and particle diameter $< 45\,\mu m$ [4].

Fig. 2 shows a schematic diagram of the collection chamber for the particles [7,8]. The particles were collected at discrete areas labeled S, PT, QB, and QP. The letter "T" represents the inner wall of the double quartz tube shown in Fig. 1, whereas QP represents the inlet port of the quench gas. The letter "S" represents the inner wall of the collection chamber, whereas QB represents the quartz board and PT represents the pyrex tube. No quenching gas was used in this study because a long plasma tail flame kept is suitable for the synthesis of $YFe_{(3+x)}O_{1.5(4+x)}$. The distance between the upper surface of QB and the ceiling board of S could be adjusted by moving QB vertically. The experiments were done at a maximum separation of 450 mm. The gas outlet port of the collection chamber was connected to a filter (F), which is not shown in Fig. 2. Ultrafine particles were also collected from this filter.

Table 1 shows the experimental conditions for different runs. The values of Fe/Y listed were determined by using inductively coupled plasma emission spectroscopy (ICP-ES). The progression from left to right shows increasing Fe/Y, except for Run E508. In Run E508, we installed another quartz tube in the collection chamber to collect particles, so that the operating conditions were different from the other runs.

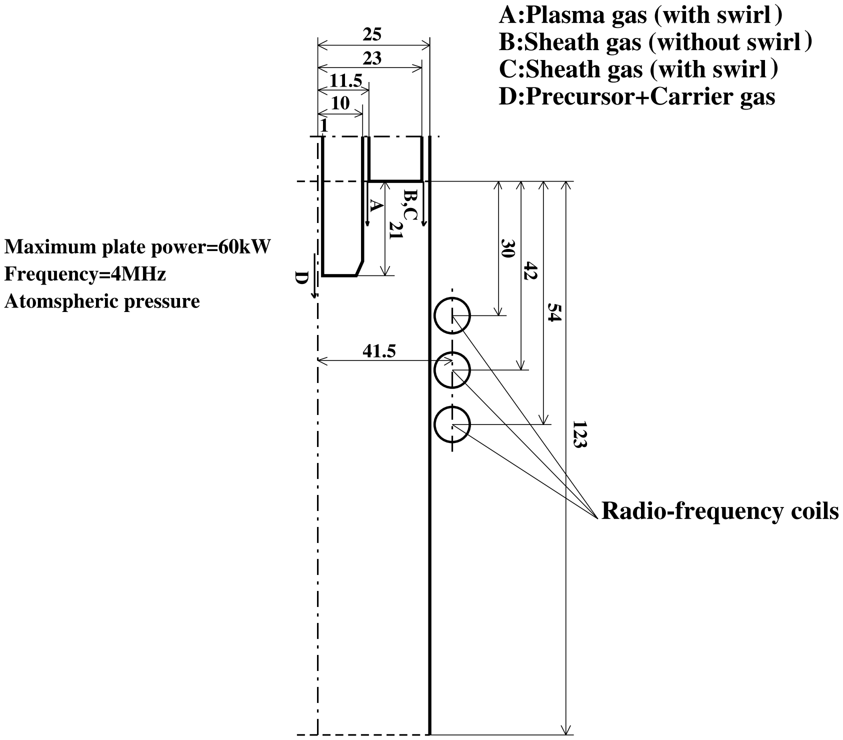

Fig. 1. Torch geometry (units: (mm)).

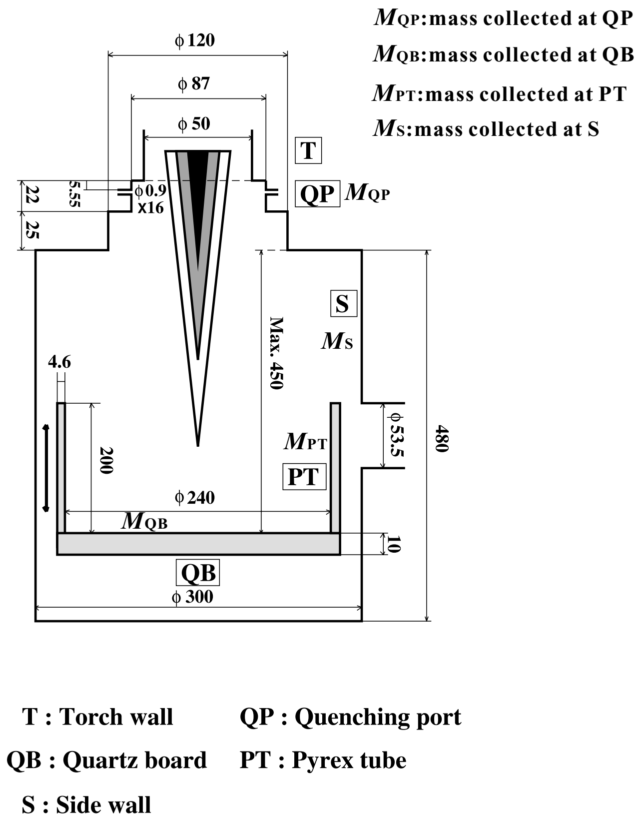

Fig. 2. Collection chamber (units: (mm)).

For all of the runs, the total gas volumetric flow rate was nearly constant. The plate power was adjusted to maintain stable plasma operation. However, feeding the precursor caused the plasma to become unstable, which made it difficult to maintain both the feed quantity and time constant over all runs. Therefore, it was impossible to maintain a constant feed rate of the precursor.

XRD analysis was used to identify the composition and crystalline structure of the synthesized ultrafine particles. Although a large quantity of $YFe_{(3+x)}O_{1.5(4+x)}$ is dissolved into HNO_3 when $YFe_{(3+x)}O_{1.5(4+x)}$-containing particles are boiled for 20 min in 2N HNO_3, h-$YFeO_3$ can be almost entirely removed [5]. Using XRD of the sample after the HNO_3 treatment, we tried to index the XRD peaks of $YFe_{(3+x)}O_{1.5(4+x)}$. Furthermore, to determine whether $YFe_{(3+x)}O_{1.5(4+x)}$ is a stoichiometric compound or whether a solid solution is formed, accurate lattice constants of $YFe_{(3+x)}O_{1.5(4+x)}$ in the individual particles collected at S were measured. A sample was prepared by applying cubic (c-)Si [9] powder (diameter $< 150\,\mu m$) to the synthesized particles in an agate mortar. The sample was then mixed by doing wet-grinding in acetone, to the extent that the Si particle diameter decreased to as small as $10\,\mu m$. XRD of these samples was done. Using the correction curve obtained from the five XRD peaks of c-Si, we corrected the XRD angles and determined the accurate cubic crystal lattice constant (a_0).

To measure the size and shape of the synthesized particles and to identify the existence of monocrystals and/or polycrystals, transmission electron microscopy (TEM)/selected-area diffraction (SAD) was used. Moreover, we examined the existence of the long periodic structure by using TEM/SAD.

Furthermore, the magnetization at room temperature and the Curie point of the synthesized particles were measured by using a vibrating sample magnetometer (VSM). Together, these measurements allowed us to determine the magnetic properties of the synthesized particles.

We also determined the magnetic properties of $YFe_{(3+x)}O_{1.5(4+x)}$ contained in the synthesized particles by using XRD, VSM, and Mössbauer spectrometry.

3. Results and discussion

3.1. Mass of collected particles

Table 2 shows the mass of collected particles at each collection area and on the filter, for five runs. Because the collection method for Run E508 was different from those used for other runs, the collected mass for Run E508 is not shown in Table 2. We describe the particles collected for Run E508 in Section 3.6.

Table 1
Experimental conditions (Y–Fe–O compounds)

	Run no.					
	E503	E403	E408	E405	E406	E508
Fe/Y (molar): precursor	2.4	3.1	3.4	3.7	4.0	1.7
A(Ar): plasma gas (slpm)	14	15	14	14	14	14
B(Ar): sheath gas (slpm)	22	22	21	23	22	22
B(O_2): sheath gas (slpm)	6	6	6	6	6	6
C(Ar): sheath gas (slpm)	23	22	23	25	23	22
C(O_2): sheath gas (slpm)	12	12	12	12	12	11
D(Ar): carrier gas (slpm)	3	3	3	3	3	3
Plate power (kW)	33.6	25.9	30.0	23.8	24.5	27.4
Feed time (min)	27.0	16.0	12.0	28.0	37.5	46.0
Feed quantity (g)	5.13	4.85	6.74	9.73	21.26	15.64
Feed rate (g/min)	0.19	0.30	0.56	0.35	0.57	0.34

Table 2
Mass of collected particles (Y–Fe–O compounds)

	Run no.				
	E503	E403	E408	E405	E406
M_{QP} (g)	0.008	0.020	0.031	0.054	0.129
M_{QB} (g)	0.008	0.002	0.006	0.004	0.004
M_{PT} (g)	0.138	0.002	0.074	0.001	–
M_S (g)	0.281	0.334	0.511	0.902	2.330
M_F[a] (g)	0.306	0.944	0.308	0.534	1.160
M_{total}[b] (g)	0.741	1.302	0.930	1.495	3.623

[a] M_F: mass collected at filter.
[b] M_{total}: total mass collected.

Increasing the mass flow of the precursor does not necessarily increase the total collected mass (M_{total}) of particles. However, for Run E406, the precursor mass flow was the highest of all runs, and the mass of particles collected at locations S and F was higher than for any other run.

3.2. Particle crystallinity

Fig. 3 shows a TEM photograph of particles collected at location S for Run E405. The particle diameters ranged from 1 to more than 100 nm. Because a large number of crystalline particles were observed, the crystallinity of the compounds synthesized in the ultrafine particles was good.

3.3. XRD identification of compounds in particles

Fig. 4 shows the XRD patterns of particles collected at location S for each of the experimental runs. In Fig. 4, the Fe/Y ratio of the precursors is shown. For all of the runs, $YFe_{(3+x)}O_{1.5(4+x)}$, h-$YFeO_3$, γ-Fe_2O_3, and ε-Fe_2O_3 [10–12] were observed in the synthesized particles. Both γ-Fe_2O_3 and ε-Fe_2O_3 are ferrimagnetic compounds.

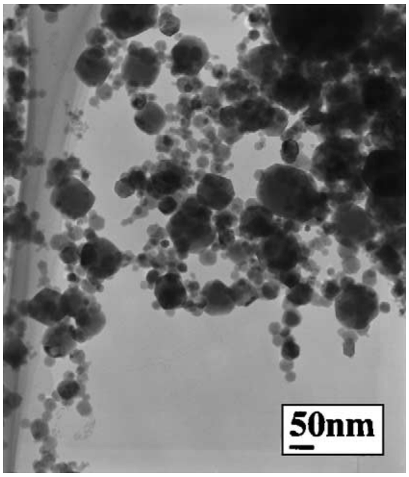

Fig. 3. TEM image of Y–Fe–O particles collected at location S for Run E405.

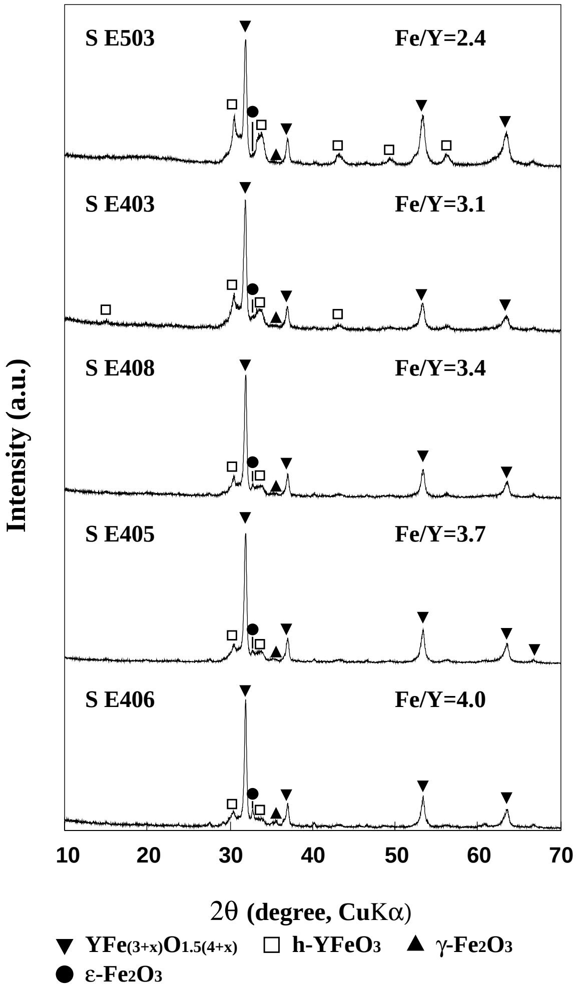

Fig. 4. XRD patterns of particles collected at location S (Y–Fe–O compounds).

With increasing Fe/Y ratio of the precursors, the XRD peak intensities of h-$YFeO_3$ decreased, and those of γ-Fe_2O_3 and ε-Fe_2O_3 increased. We have not yet determined the relation between XRD peak intensities and the quantity of these compounds. However, a proportionality exists between the intensities and the quantity. Therefore, the mass of the individual compounds synthesized is affected by the Fe/Y ratio of the precursor.

3.4. XRD and TEM/SAD analysis of crystal structure of $YFe_{(3+x)}O_{1.5(4+x)}$

Fig. 5 shows XRD of the sample obtained by boiling in HNO_3, the particles collected at location S for Run E503. Comparing the XRD pattern for the particles before the HNO_3 treatment (shown in Fig. 4), almost the entire h-$YFeO_3$ peak shown in Fig. 4 disappeared. This indicates that almost all of the h-$YFeO_3$ was removed. Despite the removal of the h-$YFeO_3$, the ε-Fe_2O_3 peaks indicated by black circles were clearly visible. This indicates that the HNO_3 treatment did not significantly remove ε-Fe_2O_3. Assuming that the XRD pattern of $YFe_{(3+x)}O_{1.5(4+x)}$ included all peaks except for ε-Fe_2O_3, indexing of $YF_{(3+x)}O_{1.5(4+x)}$

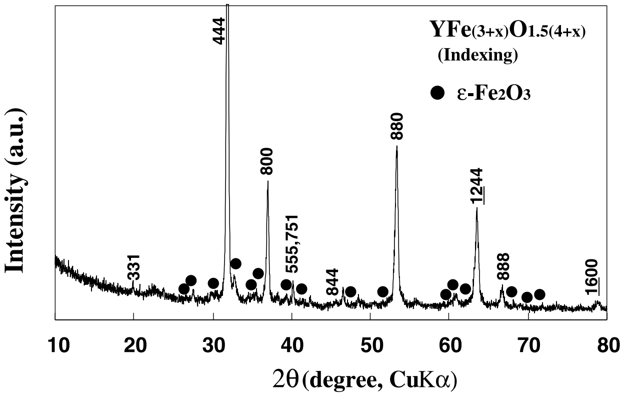

Fig. 5. XRD patterns of $YFe_{(3+x)}O_{1.5(4+x)}$ in particles collected at location S for Run E503, and purified with nitric acid.

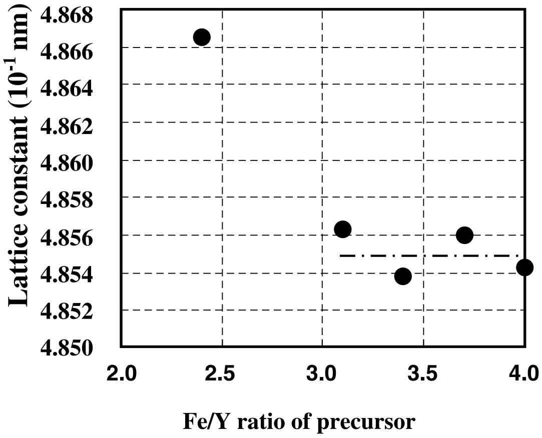

Fig. 6. Lattice constant vs. Fe/Y ratio of precursor.

was done. We previously confirmed that $YFe_{(3+x)}O_{1.5(4+x)}$ is a cubic crystal where metal atoms form face-centered cubic lattices. However, when the indices are associated with all of the peaks possibly belonging to $YFe_{(3+x)}O_{1.5(4+x)}$, the maximum peak in the vicinity of $2\theta = 31.9^\circ$ is (444), and all the indices satisfy the extinction rule of the face-centered cubic lattice.

This analysis therefore showed that $YFe_{(3+x)}O_{1.5(4+x)}$ had a sub-lattice of (111). Except for the (111) peak, the other peaks were relatively low-intensity peaks, and most of them had an asymmetric profile. For this reason, a_0 was determined only from the value of 2θ for the (111) peak of $YFe_{(3+x)}O_{1.5(4+x)}$, Fig. 6 shows the calculated values of a_0 versus the Fe/Y ratio of the precursor. Fig. 6 indicates that for $Fe/Y = 2.4$, $a_0 = 0.4867$ nm, and that for $3.1 < Fe/Y < 4.0$, $a_0 \approx 0.4855$ nm. Because these values are within the range of experimental uncertainty, they indicate that for $3.1 < Fe/Y < 4.0$, $YFe_{(3+x)}O_{1.5(4+x)}$ is a stoichiometric compound.

The maximum indexed peak was (444) with an XRD pattern of $YFe_{(3+x)}O_{1.5(4+x)}$ shown in Fig. 5, but it is still not clear if particles quenched in the plasma can assume such a long periodic structure. Fig. 7a–c shows TEM photographs and SAD patterns of ultrafine particles collected at location S for Run E405. The corresponding XRD are shown in Fig. 4. Fig. 7a shows the TEM photograph, which indicates that lattice plane spacings of 1.1 and 0.97 nm appear. Assuming that the indexing shown in Fig. 5 is correct, these lattice planes shown in Fig. 7a correspond to (111) and (200) planes, respectively. Fig. 7b shows the SAD pattern corresponding to the TEM photograph shown in Fig. 7a. By using the lattice plane spacing determined from the distances between the pivotal spot of the figure and the lattice spots, the individual lattice spots could be indexed. This analysis clearly indicates that lattice planes based on long-periodic structures such as (444), $(\underline{12}44)$, and $(\underline{16}00)$ exist. Fig. 7c shows the SAD pattern corresponding to a TEM photograph of the particles collected at location S for Run E405. In Fig. 7c, the lattice spots are arranged in a regular pattern. Assuming that the zone axis is $[01\bar{1}]$, Fig. 7c indicates that lattice spots indexed as (111), (333), and (444) existed. This confirms the existence of long-periodic structures, determined by indexing of the XRD patterns shown in Fig. 5.

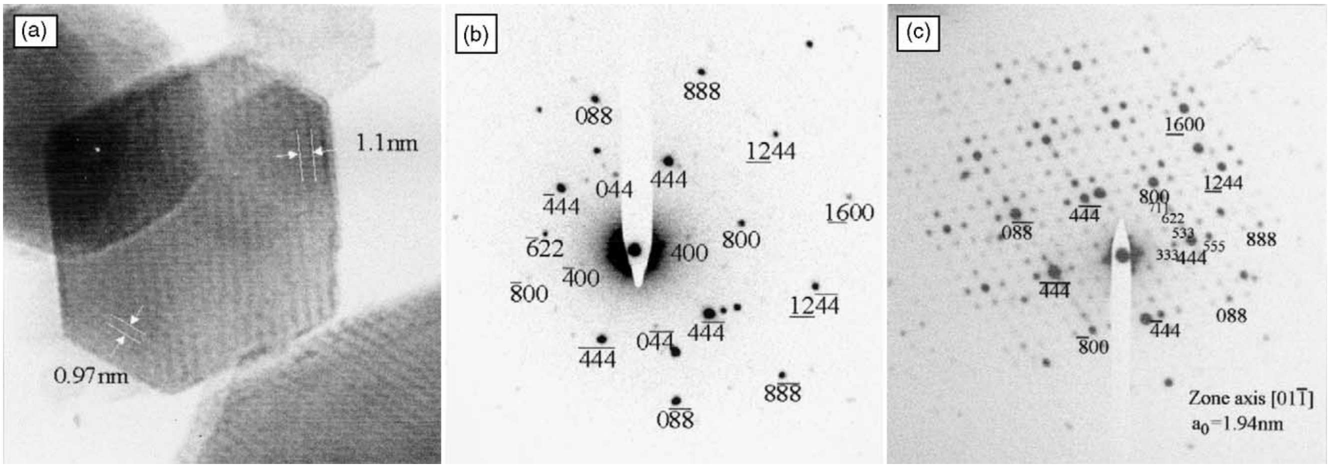

Fig. 7. TEM image of particles collected at location S for Run E405, and corresponding indexed SAD patterns. (a) TEM image of ultrafine particles. (b) Indexed SAD pattern of TEM image shown in (a). (c) Indexed SAD pattern of a TEM image other than the one shown in (a).

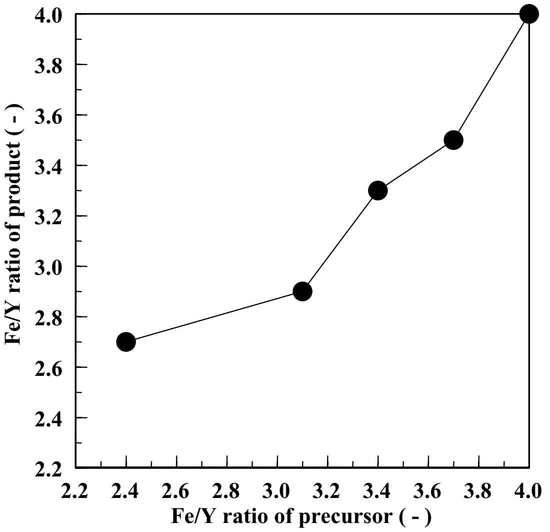

Fig. 8. Fe/Y ratio of particles vs. Fe/Y ratio of precursor.

3.5. VSM analysis of magnetic properties of particles

The synthesized Y–Fe–O particles contained ferri- or ferromagnetic substances. We determined the magnetic properties of the particles by using VSM analysis to measure their magnetization at room temperature and to measure their Curie point.

Fig. 8 shows Fe/Y of the synthesized particles versus Fe/Y of the precursor. For Fe/Y = 2.4 of the precursor, Fe/Y = 2.7 of the synthesized particles. The difference between Fe/Y of the precursor and of the particles was typically less than 12.5%. We therefore consider that Fe/Y of the synthesized particles was close to that of the precursors.

For Fe/Y of the synthesized particles shown in Fig. 8, Fig. 9 shows the saturation magnetization of the synthesized particles at room temperature. For increasing Fe/Y, the saturation magnetization increased. However, for $3.3 < \mathrm{Fe/Y} < 3.5$, the saturation magnetization was nearly constant.

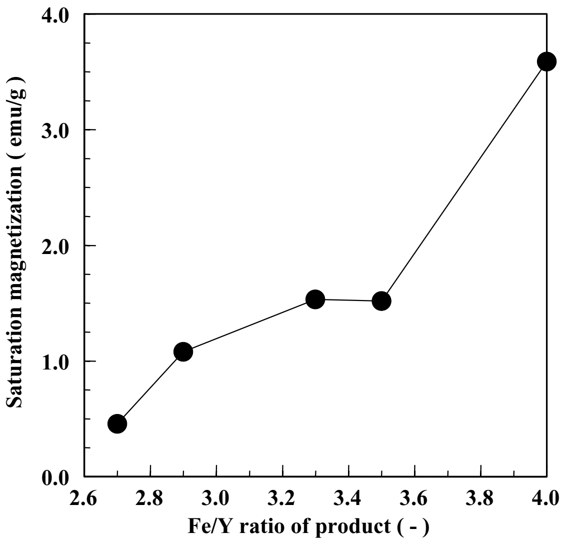

Fig. 9. Saturation magnetization vs. Fe/Y ratio of particles.

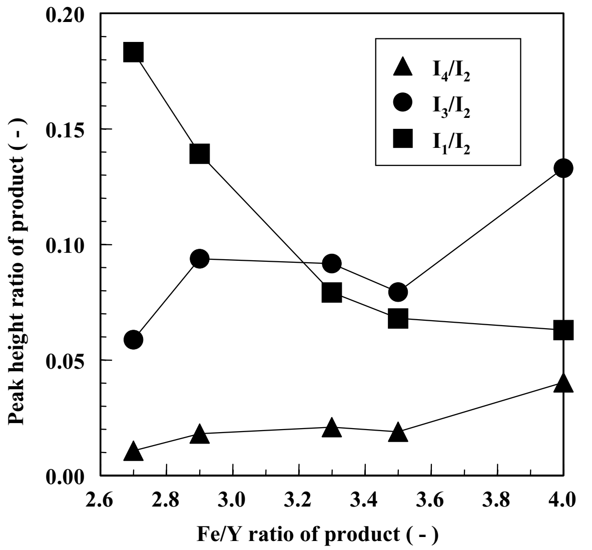

Fig. 10. Peak height ratio vs. Fe/Y ratio of particles. I_1: peak height of h-$YFeO_3$ (102). I_2: peak height of $YFe_{(3+x)}O_{1.5(4+x)}$ (444). I_3: peak height of ε-Fe_2O_3 (122). I_4: peak height of γ-Fe_2O_3 (311).

The reason for this behavior is as follows. From the XRD shown in Fig. 4, we label the peak intensity of the maximum peak (102) of h-$YFeO_3$ as I_1, that of the maximum peak (444) of $YFe_{(3+x)}O_{1.5(4+x)}$ as I_2, that of the maximum peak (122) of ε-Fe_2O_3 as I_3, and that of the maximum peak (311) of γ-Fe_2O_3 as I_4. The ratios I_1/I_2, I_3/I_2, and I_4/I_2 are therefore the relative quantities of h-$YFeO_3$, ε-Fe_2O_3, and γ-Fe_2O_3, respectively, in the synthesized particles. Fig. 10 shows the relative peak height ratio versus Fe/Y for I_1/I_2, I_3/I_2, and I_4/I_2. I_1/I_2 decreases as Fe/Y increases, which indicates that the relative quantity of h-$YFeO_3$ decreases with increasing Fe/Y. On the other hand, I_3/I_2 and I_4/I_2 increase with increasing Fe/Y. We determined that although ε-Fe_2O_3 only weakly affects the saturation magnetization at room temperature of the rare earth element–Fe–O compound, for particles synthesized by the thermal plasma evaporation method, γ-Fe_2O_3 strongly affects the saturation magnetization [8]. The tendency of I_4/I_2 increasing with increasing Fe/Y is similar to that of the saturation magnetization shown in Fig. 9. This indicates that for the Y–Fe–O system as well, that for particles synthesized by the thermal plasma evaporation method, that changing Fe/Y of the precursor affects the quantity of γ-Fe_2O_3 in the particles, which also affects their saturation magnetization at room temperature.

Fig. 11 shows the saturation magnetization versus temperature for the Curie point measurement of the particles collected at location S for Run E405, where the synthesized $YFe_{(3+x)}O_{1.5(4+x)}$ was the closest to its pure, single phase. The measurement was done under atmospheric pressure. As shown in Fig. 11, the Curie point of ε-Fe_2O_3 was 210 °C [11], whereas for γ-Fe_2O_3 it was 577 °C [13]. An

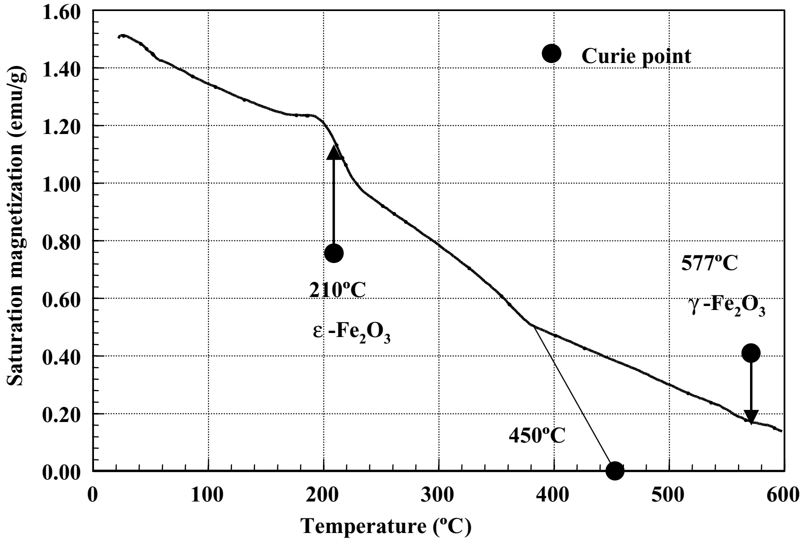

Fig. 11. Saturation magnetization vs. temperature from Curie point measurements.

inflection point also exists at 380 °C, which indicates that either a ferri- or ferromagnetic compound with a Curie point of about 450 °C may exist in the particles.

3.6. XRD, VSM, and Mössbauer analysis of magnetic properties of $YFe_{(3+x)}O_{1.5(4+x)}$

By using XRD, VSM, and Mössbauer spectrometry, we determined whether $YFe_{(3+x)}O_{1.5(4+x)}$ is either a ferri- or ferromagnetic compound.

Fig. 12 shows XRD patterns of the particles collected at location S for Run E405 and those collected at location PT for Run E508. The XRD shown in Fig. 12 indicate that for the particles collected at location S for Run E405, $YFe_{(3+x)}O_{1.5(4+x)}$ is synthesized close to a single phase. A small quantity of by-products are also indicated, such as h-$YFeO_3$, γ-Fe_2O_3, and ε-Fe_2O_3. For the particles collected at location PT for Run E508, h-$YFeO_3$ was the main product and a small quantity of $YFe_{(3+x)}O_{1.5(4+x)}$ is also indicated. From the XRD of the particles collected for Run E508, only the peaks of h-$YFeO_3$ and $YFe_{(3+x)}O_{1.5(4+x)}$ were identified.

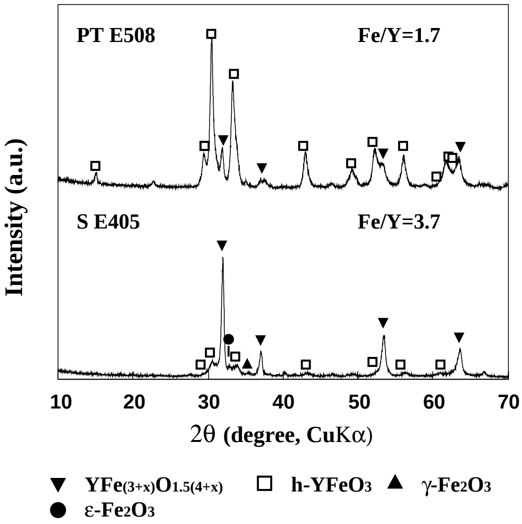

Fig. 12. XRD patterns of products containing $YFe_{(3+x)}O_{1.5(4+x)}$ and h-$YFeO_3$.

Fig. 13 shows Mössbauer spectra of the individual particles collected at location S for Run E405 (Fig. 13a) and collected at location PT for Run E508 (Fig. 13b). Two types of quadrupole and magnetic splitting appear in the spectrum of Fig. 13a, whereas only two types of quadrupole splitting appear in Fig. 13b. Assuming that a single type of quadrupole splitting corresponds to a single paramagnetic compound, Fig. 13a indicates that $YFe_{(3+x)}O_{1.5(4+x)}$ and h-$YFeO_3$ are paramagnetic compounds corresponding to the two types of quadrupole splitting, whereas γ-Fe_2O_3 and ε-Fe_2O_3 are ferrimagnetic compounds corresponding to magnetic splitting. The spectrum shown in Fig. 13b indicates that $YFe_{(3+x)}O_{1.5(4+x)}$ and h-$YFeO_3$ are paramagnetic compounds corresponding to two types of quadrupole splitting.

Table 3 shows Mössbauer parameters obtained by dividing the individual spectra into Lorenz functions. The column *area* indicates the peak area ratio, *IS* is the isomer shift, *QS* is quadrupole splitting, and *IF* is the internal magnetic field strength. The magnetic splitting of the spectrum of the particles collected at location S for Run E405 was divided into three Lorenz functions. Assuming that $YFe_{(3+x)}O_{1.5(4+x)}$ is a paramagnetic compound corresponding to a single type of *QS*, the values of *IS* and *QS* shown in Table 3 indicate that the valence of Fe in $YFe_{(3+x)}O_{1.5(4+x)}$ is +3. The stoichiometry of $YFe_{(3+x)}O_{1.5(4+x)}$ was determined by assuming that the valence of Fe is +3, because the compound was formed in a plasma where high-concentrations of oxygen existed. A valence of +3 also assumes that

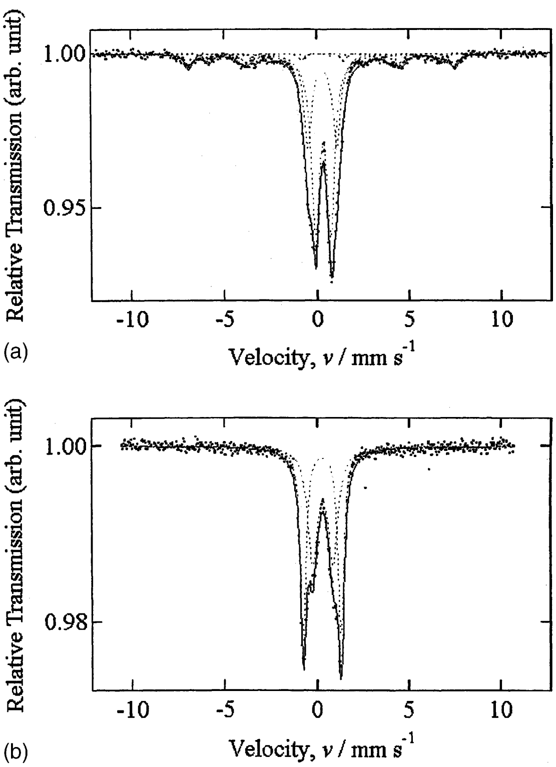

Fig. 13. Mössbauer spectra of products containing $YFe_{(3+x)}O_{1.5(4+x)}$ and h-$YFeO_3$ for particles collected at (a) location S for Run E405 and (b) location PT for Run E508.

$YFe_{(3+x)}O_{1.5(4+x)}$ is a paramagnetic compound with a single type of *QS*.

Fig. 14 shows the measured magnetization at room temperature of the particles collected at location S for Run E405. The particles were composed of either ferri- or ferromagnetic compounds, and exhibited a magnetic hysterisis curve with a saturation magnetization of 1.52 emu/g at room temperature. This coincides with the Mössbauer spectrum shown in Fig. 13a, which exhibits magnetic splitting. Because γ-Fe_2O_3 strongly affects the saturation magnetization, we also assume that γ-Fe_2O_3 also affects magnetic splitting in the Mössbauer spectrum.

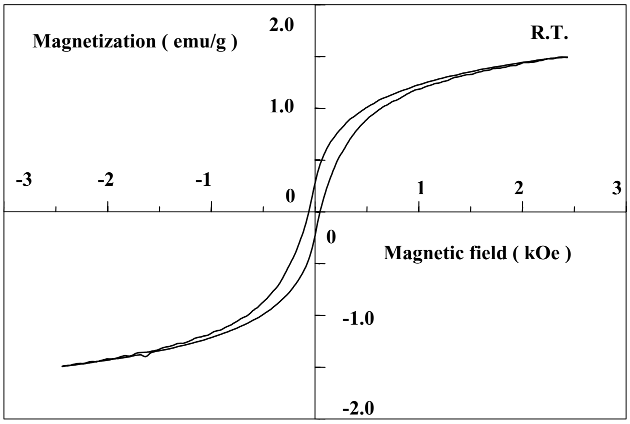

Fig. 14. Measured magnetization vs. magnetic field strength for particles collected at location S for Run E405 and containing $YFe_{(3+x)}O_{1.5(4+x)}$ and h-$YFeO_3$.

Fig. 15 shows the measured magnetization at room temperature of particles collected at location PT for Run E508. The particles were composed of either ferri- or ferromagnetic compounds, and exhibited a magnetic hysterisis curve with a saturation magnetization of 0.37 emu/g at room temperature. This behavior contradicts the result that no magnetic splitting appears in the Mössbauer spectrum shown in Fig. 13b. In the XRD shown in Fig. 12 of the particles collected at location PT for Run E508, distinct peaks corresponding to $YFe_{(3+x)}O_{1.5(4+x)}$ exist. It is therefore possible that because $YFe_{(3+x)}O_{1.5(4+x)}$ is either a ferri- or ferromagnetic compound whose saturation magnetization is very small, that the magnetic splitting is hidden in the background noise of the Mössbauer spectrum. On the other hand, it is also possible that $YFe_{(3+x)}O_{1.5(4+x)}$ is a paramagnetic compound and that a small quantity of other ferri- or ferromagnetic compounds exist in the particles. In the XRD shown in Fig. 12 for particles collected at location PT for Run E508, the peaks of h-$YFeO_3$ are broad. This implies that the peaks of these ferri- or ferromagnetic compounds are hidden.

Table 3
Mössbauer parameters of products containing $YFe_{(3+x)}O_{1.5(4+x)}$ and h-$YFeO_3$

Sample	Partial	Area (%)	*IS* (mm/s)	*QS* (mm/s)	*IF* (T)
S E405	1	54.3	0.35	0.85	–
	2	29.2	0.32	1.59	–
	3	8.8	0.33	−0.04	44.8
	4	5.1	0.41	0.04	39.0
	5	2.6	0.16	0.25	27.9
PT E508	1	65.7	0.28	2.02	–
	2	34.3	0.33	0.99	–

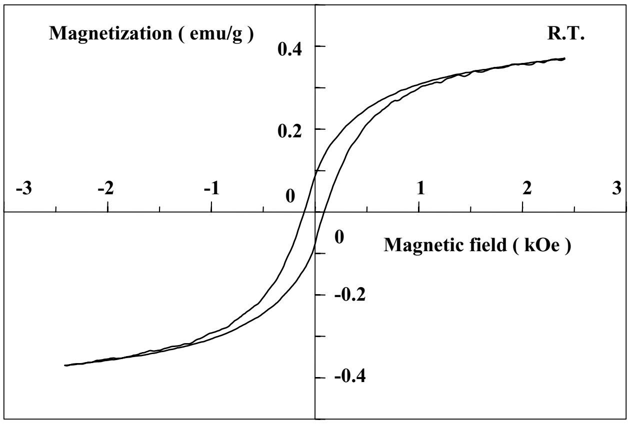

Fig. 15. Measured magnetization vs. magnetic field strength for particles collected at location PT for Run E508 and containing $YFe_{(3+x)}O_{1.5(4+x)}$ and h-$YFeO_3$.

Although Mössbauer spectrometry suggests that $YFe_{(3+x)}O_{1.5(4+x)}$ is a paramagnetic compound, it was impossible to confirm this based on VSM measurements.

4. Conclusions

We used an rf Ar–O_2 thermal plasma to synthesize ultrafine particles composed of Y–Fe–O compounds. From our analysis of the particles we conclude that

(1) A new compound was identified in the particles: $YFe_{(3+x)}O_{1.5(4+x)}$. It is a cubic crystal where face-centered cubic lattices are formed by metal atoms, and has long-period structures with (444) maximum XRD peaks.
(2) The synthesized particles were either ferri- or ferromagnetic at room temperature. A small quantity of γ-Fe_2O_3 contained in the particles strongly affects the saturation magnetization at room temperature.
(3) To determine whether $YFe_{(3+x)}O_{1.5(4+x)}$ is a ferri-, ferro-, or paramagnetic compound, particles with a large quantity of $YFe_{(3+x)}O_{1.5(4+x)}$ and with a minimum of other ferri- or ferromagnetic by-products are needed.

References

[1] T. Kanou, H. Yanaghida, Rare Earths—Properties and Applications, Gihoudou Shuttpan, Tokyo, 1980.
[2] M. Douyama, Reametaru Jiten, Fuji Tekunoshisutemu, Tokyo, 1991.
[3] M. Sugasawa, N. Kikukawa, N. Ishikawa, J. Soc. Powder Technol., Jpn. 32 (1995) 660–667 (in Japanese).
[4] M. Sugasawa, N. Kikukawa, N. Ishikawa, N. Kayano, T. Kimura, J. NIRE 6 (1997) 231–240 (in Japanese).
[5] M. Sugasawa, N. Kikukawa, N. Ishikawa, N. Kayano, T. Kimura, Resour. Process. 44 (1997) 74–79 (in Japanese).
[6] M. Sugasawa, N. Kikukawa, N. Ishikawa, N. Kayano, T. Kimura, J. Aerosol Sci. 29 (1998) 675–686.
[7] M. Sugasawa, N. Kikukawa, N. Kayano, T. Kimura, J. Aerosol Res., Jpn. 15 (2000) 264–272 (in Japanese).
[8] M. Sugasawa, N. Kikukawa, Y. Nagano, N. Kayano, T. Kimura, J. Soc. Powder Technol., Jpn 40 (2003) 920–928 (in Japanese).
[9] Powder Diffraction File No. 5-565, PDF-International Center for Diffraction Data.
[10] V.R. Schrader, G. Büttner, Z. Anorg. Allgem. Chem. 320 (1963) 220–234 (in German).
[11] E. Tronc, C. Chanéac, J.P. Jolivet, J. Solid State Chem. 139 (1998) 93–104.
[12] D. Nižňaský, A. Lančok, A. Hutlová, J. Buršík, J.L. Rehspringer, Int. J. Inorg. Mater. 3 (2001) 479–483.
[13] Ouyou Busturi Gakukai, Ouyoubusturi Data Book, Maruzen, Tokyo, 1994.